

DECEMBER 19 2023

## Low-frequency radiation from a vibrating cap on a rigid spherical shell with a circular aperture

Samuel D. Bellows  ; Timothy W. Leishman



*J. Acoust. Soc. Am.* 154, 3883–3898 (2023)

<https://doi.org/10.1121/10.0023936>

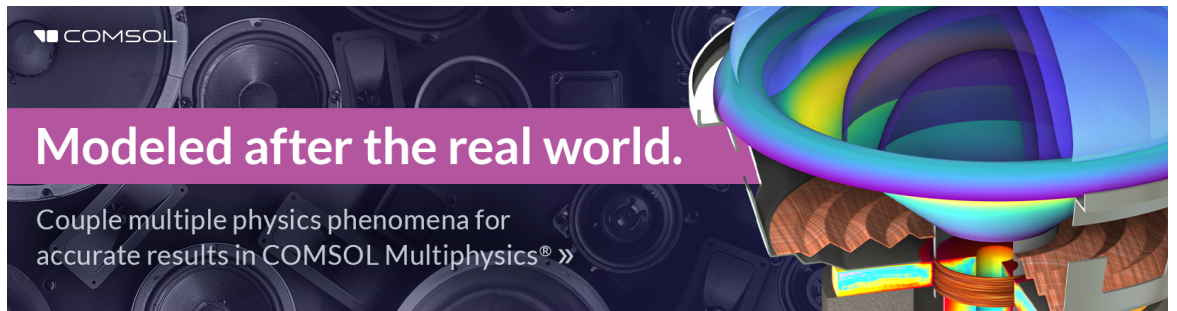


View  
Online



Export  
Citation

CrossMark



 **Modeled after the real world.**

Couple multiple physics phenomena for accurate results in COMSOL Multiphysics® »

## Low-frequency radiation from a vibrating cap on a rigid spherical shell with a circular aperture

Samuel D. Bellows<sup>a)</sup>  and Timothy W. Leishman

*Acoustics Research Group, Brigham Young University, Provo, Utah 84602, USA*

### ABSTRACT:

Theoretical models based on spherical geometries have long provided essential insights into the directional behavior of sound sources such as loudspeakers and human speech. Because commonly applied models predict omnidirectional radiation at low frequencies and increasing directionality at higher frequencies, they fail to predict the directional characteristics of certain sources with different source geometries. These sources include violins and open-back guitar amplifiers that have openings or ports connecting a cavity or enclosure to the exterior domain. This work presents the low-frequency radiation from a vibrating cap on a rigid spherical shell with a circular aperture to study the directional characteristics of such sources. The proposed model predicts dipolar radiation at very low frequencies, monopolar radiation near the Helmholtz resonance, and increasing directionality at higher frequencies. Experimental results based on measuring the sound field of an open-back spherical loudspeaker validate the theoretical model and highlight its utility in predicting directional behavior. © 2023 Acoustical Society of America.

<https://doi.org/10.1121/10.0023936>

(Received 29 June 2023; revised 21 October 2023; accepted 20 November 2023; published online 19 December 2023)

[Editor: Wonkyu Moon]

Pages: 3883–3898

### I. INTRODUCTION

Theoretical models based on simple spherical geometries have long been used to improve understanding of the directional characteristics of sound sources. Their usefulness primarily results from their geometries, which allow spherical harmonic expansions of the pressure field with analytically determined expansion coefficients. The advantage of spherical models over the circular cap in an infinite plane rigid baffle and its counterparts<sup>1–3</sup> is that they incorporate diffraction about finite bodies, yielding more realistic approximations over three-dimensional space for practical applications. Consequently, spherical models are desirable for their reliability, computational clarity, and increased realism.

Morse and Ingard derived analytical results for a radially vibrating “cap” (spherical cap or spherical segment of one base) and a point source on a rigid sphere.<sup>4,5</sup> Among other effects, their results showed omnidirectional radiation for long wavelengths and shadowing behind the sphere, both of which are helpful for understanding basic diffraction effects ranging from those of loudspeaker cabinets<sup>6</sup> to musicians’ bodies.<sup>7</sup> Skudrzyk derived results for an axially vibrating spherical cap and a plane circular cap set in a sphere.<sup>8</sup> The latter employed a least squares approximation to the expansion coefficients based on a technique developed by Williams *et al.*<sup>9</sup> Beranek and Mellow considered radiation from a rectangular cap on a sphere,<sup>10</sup> with results that required numerical integration to determine the final values of the expansion coefficients. Aarts and Janssen

provided results for axisymmetric velocity distributions by introducing the Zernike polynomials to provide solutions for various Stenzel velocity profiles.<sup>11</sup> Other authors have explored variations such as surrounding a vibrating cap with a pressure-release spherical baffle<sup>12</sup> or surrounding a vibrating cap with a pressure-release belt set in a rigid spherical baffle.<sup>13</sup>

Numerous authors have applied spherical models successfully to predict directivities of practical sources. For example, Johansen found in his horn studies that a radially oscillating cap set in a rigid sphere provided excellent agreement with his boundary element method (BEM) simulations.<sup>14</sup> Other authors implemented spherical models to simulate the directivities of regular polyhedron loudspeakers (RPLs).<sup>15–17</sup> Through superposition, one can easily place multiple vibrating caps, representing loudspeaker drivers of varying sizes and locations, on an otherwise rigid spherical body. When they are combined in this way, the resultant directivities no longer produce a single axis of principal radiation at small wavelengths but instead take on more complex multi-directional patterns characteristic of RPLs.<sup>18</sup> Beyond loudspeakers, authors have employed the model of a radially vibrating cap on a sphere to represent the radiation and directivity of speech.<sup>19–21</sup>

While each spherical model has included different underlying assumptions about the cap velocity distribution or boundary conditions on the spherical baffle, they all qualitatively suggest the same general directional characteristics: (1) omnidirectional radiation for long wavelengths and (2) strong directivity in front of the vibrating cap with accompanying shadowing behind the sphere for short wavelengths. Consequently, despite their broad applicability and utility in

<sup>a)</sup>Email: samuel.bellows11@gmail.com

approximating selected source radiation characteristics, they cannot satisfactorily represent other sources without further adaptations. For example, more challenging problems include some ported loudspeakers, open-back guitar amplifiers, and many musical instruments that may not behave as omnidirectional sources at low frequencies. Their lack of omnidirectional behavior is due to the “sound hole sum rule” discussed by Weinreich in his work on the violin.<sup>22</sup>

The sound hole sum rule states that when the wavelength is large so that the air motion behaves as an incompressible fluid, source geometries with ports or sound holes connecting the interior cabinet or cavity to the exterior domain have a vanishing monopole moment. This effect occurs as any incompressible flow produced by a vibrating surface is exactly canceled by flow entering through the opening. This volume velocity cancellation allows more complex radiation patterns at low frequencies, such as dipolar radiation for the violin. As a monopole moment can only form when inertial effects disrupt the exact cancellation of the velocity flow, the Helmholtz resonance of such configurations demarcates varying directional behavior.<sup>22</sup>

Previous works have considered geometries relevant to these problems to a limited extent, although they primarily focused on sound scattering. For example, Miles explored the scattering of a plane wave by a hollow, rigid spherical shell with a circular aperture.<sup>23</sup> Because the resultant boundary value problem (BVP) led to mixed boundary conditions, he presented both a long wavelength approximation and numerically evaluated variational solutions. Elias and Malb eque considered scattering from a point source located at the center of a similar structure using both the BEM and the method of analytical reduction (MAR),<sup>24</sup> a valuable technique for efficient solutions with both long and short wavelengths.<sup>25</sup> Their results included an analysis of the Helmholtz resonance, radiated sound power, and directivity. More recently, Vinogradova considered scattering from a spherical barrel (a hollow sphere with two circular apertures), also using MAR.<sup>26</sup>

Despite its potential to support many modeling applications, one arrangement lacks significant analysis in the literature: the sound radiation from a vibrating cap set on a rigid spherical shell with an open circular aperture. Knowledge of the solution to this problem will benefit researchers and practitioners in several areas of acoustics, whose explorations include relevant vibrations and radiations from cavity-like structures with apertures.

This work develops a solution in the following ways. First, Sec. II presents the problem formulation and derives two integral equations that solve the BVP, following the general approach used by Miles. The first equation, based on an aperture-velocity formulation, is most useful when the aperture size is smaller than the wavelength. The second equation, based on a potential-layer formulation, reduces to thin-walled boundary integral equations and is more suitable for larger aperture sizes.

While one may discretize both integral equations and numerically solve them using BEMs, Sec. III instead

focuses on a low-frequency approximation based on the concepts of self- and mutual radiation impedances between the vibrating cap and aperture. While numerical methods are commonly used in acoustics to solve complex problems, Shaw noted that “the cost is high in terms of effort and in the loss of contact with fundamental concepts.”<sup>27</sup> The low-frequency approximation leads to a superposition of two caps on a rigid sphere, one of whose velocity is the given vibrating cap velocity and the other is the aperture particle velocity. Analytical solutions to the self- and mutual impedances reveal that these two equivalent caps vibrate out of phase at very low frequencies and in phase at the Helmholtz resonance frequency.

Further simplification of the self- and mutual impedances leads to their lumped-element approximations, including the interior and exterior end corrections for a cap set in a sphere. The lumped element parameters predict essential system characteristics, including the Helmholtz resonance. A multipole expansion of the radiation reveals the low-frequency directional characteristics, including dipole radiation at large wavelengths and quasi-omnidirectionality at the Helmholtz resonance frequency. Finally, Sec. V validates the results experimentally through directivity measurements of a spherical loudspeaker with a single driver and a variable enclosure aperture.

## II. ANALYTICAL MODEL

### A. Formulation

Consider a rigid, spherical shell of radius  $r = a$  and negligible wall thickness, as depicted in Fig. 1. The shell includes a circular aperture of cone half angle  $\alpha_a$  centered about  $(\theta_a, \phi_a)$ . It also includes a radially vibrating spherical cap of cone half angle  $\alpha_c$  centered about  $(\theta_c, \phi_c)$  with constant normal surface velocity  $u_c$ .

Denote the exterior domain  $\Omega^+$  as the region  $r > a$  and the interior domain  $\Omega^-$  as the region  $r < a$ . Additionally, let  $\Gamma_c$  be the surface of the vibrating cap,  $\Gamma_a$  be the spherical surface of the aperture, and  $\Gamma_s$  be the surface of the remaining spherical shell.

The following BVP describes the time-harmonic pressure (for  $e^{i\omega t}$  time dependence):

$$\nabla^2 p(r, \theta, \phi) + k^2 p(r, \theta, \phi) = 0, \quad \Omega^+, \Omega^-, \quad (1)$$

$$\lim_{r \rightarrow \infty} \left( r \left[ \frac{\partial}{\partial r} p(r, \theta, \phi) + ikp(r, \theta, \phi) \right] \right) = 0, \quad (2)$$

$$u_n(a, \theta, \phi) = \begin{cases} u_c, & \Gamma_c, \\ 0, & \Gamma_s, \end{cases} \quad (3)$$

$$p^+(a, \theta, \phi) = p^-(a, \theta, \phi), \quad \Gamma_a, \quad (4)$$

$$u_n^+(a, \theta, \phi) = u_n^-(a, \theta, \phi), \quad \Gamma_a, \quad (5)$$

where  $u_n$  is the particle velocity normal to the spherical surface. Equation (2) represents the Sommerfeld radiation condition [see Ref. 28, Eq. (4.5.5)] and Eqs. (4) and (5),

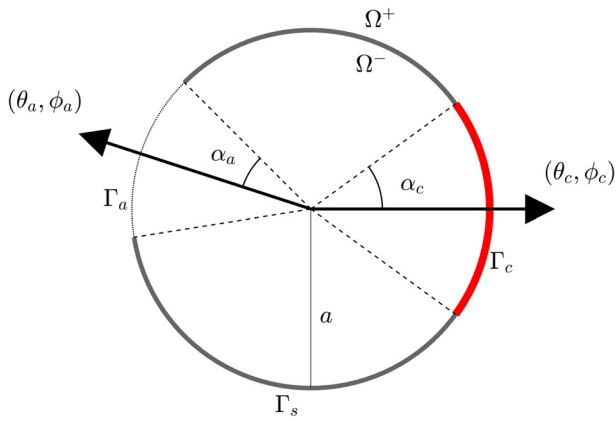


FIG. 1. (Color online) Depiction of a vibrating cap (red) on a rigid spherical shell (gray) with an open aperture.

respectively, enforce the continuities of pressure and particle velocity across the aperture connecting the interior and exterior domains.

The following presents two distinct integral equations that solve the BVP, reflecting the general approach of Miles. The first follows from an aperture velocity formulation, whereas the second employs a potential-jump formulation across the surface at  $r = a$ . The work presents both methods because the first leads to a low-frequency approximation derived later; the second relates to common boundary integral equations.

### B. Aperture velocity solution

One approach to the solution is to superpose two rigid, closed spheres with vibrating caps, as in techniques used to model RPLs and their directivities.<sup>15-17</sup> The first cap's normal velocity  $u_c$  is constant and the second cap's normal velocity  $u_a(\theta, \phi)$  is the unknown aperture particle velocity, which generally varies over  $\Gamma_a$  and satisfies the remaining boundary conditions. The total pressure from both caps is

$$p(\mathbf{r}) = p_1(\mathbf{r}) + p_2(\mathbf{r}), \tag{6}$$

where  $p_1$  is the pressure produced by the sphere with cap velocity  $u_c$  and  $p_2$  is the pressure produced by the sphere with cap velocity (aperture particle velocity)  $u_a(\theta, \phi)$ .

An eigenfunction expansion yields the pressure  $p_1$  for a radially vibrating cap on a rigid sphere. Expanding the associated particle velocity  $u_1$  in terms of spherical harmonics gives

$$u_1(\theta, \phi) = \sum_{n=0}^{\infty} \sum_{m=-n}^n U_n^m Y_n^m(\theta, \phi), \tag{7}$$

where

$$Y_n^m(\theta, \phi) = \sqrt{\frac{(2n+1)(n-m)!}{4\pi(n+m)!}} P_n^m(\cos \theta) e^{im\phi} \tag{8}$$

are the normalized spherical harmonics of degree  $n$  and order  $m$  (Ref. 29) and

$$U_n^m = u_c A_n(\alpha_c) \frac{4\pi}{(2n+1)} [Y_n^m(\theta_c, \phi_c)]^*, \tag{9}$$

where the asterisk denotes complex conjugation. The coefficients  $A_n$  are<sup>10</sup>

$$A_n(\alpha_c) = \begin{cases} \frac{1}{2}(1 - \cos \alpha_c), & n = 0, \\ \frac{1}{2}[P_{n-1}(\cos \alpha_c) - P_{n+1}(\cos \alpha_c)], & n > 0, \end{cases} \tag{10}$$

where  $P_n$  are the Legendre polynomials, such that

$$\sum_{n=0}^{\infty} A_n(\alpha_c) P_n(\cos \theta) = \begin{cases} 1, & \theta < \alpha_c, \\ 0, & \theta > \alpha_c. \end{cases} \tag{11}$$

Additionally, the surface area of a cap of angle  $\alpha_c$  is

$$S_c = 2\pi a^2 (1 - \cos \alpha_c). \tag{12}$$

Equation (10) provides the Legendre polynomial expansion coefficients of a unit amplitude cap for the axisymmetric case  $(\theta_c, \phi_c) = (0, 0)$ ,  $u_c = 1$ . Equation (9) then applies the spherical harmonic addition theorem<sup>29</sup>

$$P_n(\cos \Theta) = \frac{4\pi}{2n+1} \sum_{m=-n}^n Y_n^m(\theta, \phi) [Y_n^m(\theta_c, \phi_c)]^*, \tag{13}$$

where  $\cos \Theta = \cos \theta \cos \theta_c + \sin \theta \sin \theta_c \cos(\phi - \phi_c)$  with  $\Theta$  being the angle between  $(\theta, \phi)$  and  $(\theta_c, \phi_c)$ , to rotate the vibrating cap to arbitrary  $(\theta_c, \phi_c)$ .

The velocity expansion coefficients  $U_n^m$  not only determine the normal velocity over the sphere but also uniquely define the radiated pressure field.<sup>39</sup> Applying Euler's equation on the spherical surface

$$-iz_0 k u_1(\theta, \phi) = \frac{\partial}{\partial r} p_1(r, \theta, \phi) \Big|_{r=a} \tag{14}$$

to the solution of the Helmholtz equation in spherical coordinates gives the pressure both inside and outside the sphere as [see Ref. 39, Eq. (6.96) and Eq. (6.102) and compare Ref. 23, Eq. (18)]

$$p_1(r, \theta, \phi) = \begin{cases} -iz_0 \sum_{n=0}^{\infty} \sum_{m=-n}^n U_n^m \frac{j_n(kr)}{j_n'(ka)} Y_n^m(\theta, \phi), & r < a, \\ -iz_0 \sum_{n=0}^{\infty} \sum_{m=-n}^n U_n^m \frac{h_n^{(2)}(kr)}{h_n^{(2)'}(ka)} Y_n^m(\theta, \phi), & r > a, \end{cases} \tag{15}$$

where  $j_n$  and  $h_n^{(2)}$  are the spherical Bessel and Hankel functions of order  $n$  and  $z_0 = \rho_0 c$  is the characteristic specific acoustic impedance of the medium.

The pressure  $p_2$  produced by the second cap representing the aperture particle velocity follows similarly. The spherical harmonic expansion coefficients relate to  $u_a(\theta, \phi)$  through the orthogonality of the spherical harmonics

$$V_n^m = \int_0^{2\pi} \int_0^\pi u_a(\theta, \phi) [Y_n^m(\theta, \phi)]^* \sin \theta d\theta d\phi. \quad (16)$$

The integral vanishes outside of  $\Gamma_a$  and the resultant pressure is

$$p_2(r, \theta, \phi) = \begin{cases} -iz_0 \sum_{n=0}^{\infty} \sum_{m=-n}^n V_n^m \frac{j_n(kr)}{j_n'(ka)} Y_n^m(\theta, \phi), & r < a, \\ -iz_0 \sum_{n=0}^{\infty} \sum_{m=-n}^n V_n^m \frac{h_n^{(2)}(kr)}{h_n^{(2)'}(ka)} Y_n^m(\theta, \phi), & r > a. \end{cases} \quad (17)$$

Continuity boundary conditions across the aperture determine  $u_a(\theta, \phi)$  and its expansion coefficients  $V_n^m$ . To derive the result, first let  $\delta p_1$  be the pressure difference of  $p_1$  across the boundary  $r = a$  of the closed sphere with a radially vibrating cap

$$\delta p_1(\theta, \phi) = -iz_0 \sum_{n=0}^{\infty} \sum_{m=-n}^n \zeta_n U_n^m Y_n^m(\theta, \phi), \quad (18)$$

where, with the aid of the Wronskian relationship

$$j_n'(ka)h_n(ka) - h_n'(ka)j_n(ka) = \frac{i}{(ka)^2}, \quad (19)$$

the expansion coefficient is

$$\zeta_n = \frac{i}{j_n'(ka)h_n'(ka)(ka)^2}. \quad (20)$$

The pressure difference  $\delta p_2$  caused by the aperture cap has a form similar to Eq. (18) but with  $U_n^m$  replaced by  $V_n^m$ . The total pressure difference  $\delta p$  from both fields is then

$$\begin{aligned} \delta p(\theta, \phi) &= \delta p_1(\theta, \phi) + \delta p_2(\theta, \phi) \\ &= \delta p_1(\theta, \phi) - iz_0 \sum_{n=0}^{\infty} \sum_{m=-n}^n \zeta_n V_n^m Y_n^m(\theta, \phi). \end{aligned} \quad (21)$$

Applying continuity of pressure ( $\delta p = 0$ ) at the boundary yields

$$iz_0 \sum_{n=0}^{\infty} \sum_{m=-n}^n \zeta_n V_n^m Y_n^m(\theta, \phi) = \delta p_1(\theta, \phi), \quad (\theta, \phi) \in \Gamma_a, \quad (22)$$

so that substituting Eq. (16) into Eq. (22) gives the integral equation

$$\begin{aligned} \iint_{\Gamma_a} u_a(\theta', \phi') K_a(\cos \Theta) \sin \theta' d\theta' d\phi' \\ = \delta p_1(\theta, \phi), \quad (\theta, \phi) \in \Gamma_a, \end{aligned} \quad (23)$$

where

$$K_a(\cos \Theta) = iz_0 \sum_{n=0}^{\infty} \zeta_n \frac{2n+1}{4\pi} P_n(\cos \Theta). \quad (24)$$

The integral equation only requires evaluation on  $\Gamma_a$ . Equation (23) corresponds to Eq. (26) of Ref. 23, except with a different definition of  $\delta p$  because Miles' formulation considered the pressure jump due to a plane wave and not a vibrating cap on a rigid sphere. Standard numerical procedures can discretize and solve the integral equation for  $u_a$  since  $K_a$  and  $\delta p_1$  are known.<sup>23,30</sup>

### C. Potential layer solution

The potential layer approach determines the pressure as a result of a pressure jump  $\delta p$  across the spherical boundary  $r = a$ . Expressing the potential layer  $\delta p$  in terms of a spherical harmonic expansion and then applying Euler's equation and the associated boundary conditions yields another integral equation, this time over  $\Gamma_c \cup \Gamma_s$  (Ref. 23),

$$\begin{aligned} \iint_{\Gamma_c \cup \Gamma_s} \delta p(\theta', \phi') g_s(\cos \Theta) \sin \theta' d\theta' d\phi' \\ = iz_0 u_n(\theta, \phi), \quad (\theta, \phi) \in \Gamma_c \cup \Gamma_s, \end{aligned} \quad (25)$$

where

$$g_s(\cos \Theta) = \sum_{n=0}^{\infty} \zeta_n^{-1} \frac{2n+1}{4\pi} P_n(\cos \Theta). \quad (26)$$

This integral equation coincides with Eq. (57) of Ref. 23.

Given the expression for the free-space Green's function in terms of spherical harmonics<sup>23</sup>

$$G(\mathbf{r}, \mathbf{r}') = - \sum_{n=0}^{\infty} ikh_n^{(2)}(kr) j_n(kr') \frac{2n+1}{4\pi} P_n(\cos \Theta), \quad (27)$$

when  $\mathbf{r}$  and  $\mathbf{r}'$  are on the surface  $r = a$ ,

$$\frac{\partial^2}{\partial r \partial r'} G(\mathbf{r}, \mathbf{r}') = - \frac{k}{a^2} g_s(\cos \Theta) \quad (28)$$

and one obtains

$$\iint_{\Gamma_c \cup \Gamma_s} \delta p(\mathbf{r}') \frac{\partial^2}{\partial n \partial n'} G(\mathbf{r}, \mathbf{r}') dS = -iz_0 k u_n(\mathbf{r}), \quad (29)$$

which is a thin-body formulation of the hyper-singular boundary integral equation.<sup>31-33</sup> Reference 30 contains more details concerning its numerical implementation and the necessary handling of the kernel's singularities.

Importantly, one solves Eq. (23) over  $\Gamma_a$  whereas one solves Eq. (29) over  $\Gamma_c \cup \Gamma_s$ . Consequently, when considering the total number of discretized unknowns, Eq. (23) is more appropriate for a small aperture size, whereas Eq. (29) is more appropriate for a large aperture size.

## III. LOW-FREQUENCY APPROXIMATIONS

### A. Vibrating cap self-and mutual impedance

Consider the aperture velocity formulation presented in Sec. II B. Assuming the aperture velocity is roughly constant

at low frequencies allows a simplified approximation based on the superposition of two radially vibrating caps on a sphere. Determining the aperture velocity amplitude requires the self-and mutual impedances between these two caps. Consequently, this section develops the self-and mutual impedances between two radially vibrating caps on a sphere. The first has a cone half angle  $\alpha_1$  and surface area  $S_1$ , while the second has a cone half angle  $\alpha_2$  and surface area  $S_2$ .

On the exterior side, the self-acoustic impedance of the first cap is<sup>10,34</sup>

$$Z_{A,11}^+ = \frac{\langle p_1 \rangle_{S_1}^+}{U_1} \Big|_{U_2=0} = \frac{-i4\pi a^2 z_0}{S_1^2} \sum_{n=0}^{\infty} \frac{h_n^{(2)}(ka)}{h_n^{(2)'}(ka)} \frac{A_n^2(\alpha_1)}{(2n+1)}. \quad (30)$$

On the interior side, the self-impedance follows by replacing the spherical Hankel functions with spherical Bessel functions,

$$Z_{A,11}^- = \frac{\langle p_1 \rangle_{S_1}^-}{U_1} \Big|_{U_2=0} = \frac{-i4\pi a^2 z_0}{S_1^2} \sum_{n=0}^{\infty} \frac{j_n(ka)}{j_n'(ka)} \frac{A_n^2(\alpha_1)}{(2n+1)}. \quad (31)$$

The self-impedances of the second cap follow similarly.

The exterior mutual acoustic impedance between the first and second caps is<sup>34</sup>

$$\begin{aligned} Z_{A,12}^+ &= \frac{\langle p_1 \rangle_{S_1}^+}{U_2} \Big|_{U_1=0} \\ &= \frac{-i4\pi a^2 z_0}{S_1 S_2} \sum_{n=0}^{\infty} P_n(\cos \Theta_{12}) \\ &\quad \times \frac{h_n^{(2)}(ka)}{h_n^{(2)'}(ka)} \frac{A_n(\alpha_1) A_n(\alpha_2)}{(2n+1)}, \end{aligned} \quad (32)$$

where  $\Theta_{12}$  is the angle between the centers of the two caps. For the interior side, the mutual impedance is

$$\begin{aligned} Z_{A,12}^- &= \frac{\langle p_1 \rangle_{S_1}^-}{U_2} \Big|_{U_1=0} \\ &= \frac{-i4\pi a^2 z_0}{S_1 S_2} \sum_{n=0}^{\infty} P_n(\cos \Theta_{12}) \\ &\quad \times \frac{j_n(ka)}{j_n'(ka)} \frac{A_n(\alpha_1) A_n(\alpha_2)}{(2n+1)}. \end{aligned} \quad (33)$$

The mutual impedances  $Z_{A,21}^+ = Z_{A,12}^+$  and  $Z_{A,21}^- = Z_{A,12}^-$  from acoustic reciprocity, which is apparent from the formulas.

### B. Approximation using eigenfunction expansion

At low frequencies, the self-and mutual impedances relate the cap volume velocity  $U_c = u_c S_c$  to the unknown aperture volume velocity  $U_a$  in the following way. The total spatially averaged pressure at the aperture opening due to both caps is

$$\langle p_a \rangle_{S_a}^{\pm} = U_a Z_{A,aa}^{\pm} + U_c Z_{A,ac}^{\pm}, \quad (34)$$

where  $Z_{A,aa}$  is the self-impedance,  $Z_{A,ac}$  is the mutual impedance, and the  $\pm$  symbol indicates that the expression holds for both the exterior and interior sides. Replacing the pointwise continuity of the pressure [Eq. (4)] with continuity of the spatially averaged pressure requires that

$$U_a = -U_c \left( \frac{Z_{A,ac}^+ - Z_{A,ac}^-}{Z_{A,aa}^+ - Z_{A,aa}^-} \right). \quad (35)$$

Thus, under the approximation of uniform aperture particle velocity ( $u_a S_a = U_a$ ), the low-frequency representation of  $V_n^m$  becomes

$$V_n^m \approx u_a \frac{4\pi A_n(\alpha_a)}{(2n+1)} [Y_n^m(\theta_a, \phi_a)]^*. \quad (36)$$

The total pressure field becomes

$$p(r, \theta, \phi, k) = \sum_{n=0}^{\infty} \sum_{m=-n}^n G_n^m(k) h_n^{(2)}(kr) Y_n^m(\theta, \phi), \quad (37)$$

where

$$\begin{aligned} G_n^m &= \frac{-iz_0}{h_n^{(2)'}(ka)} \frac{4\pi}{(2n+1)} \left\{ u_c A_n(\alpha_c) [Y_n^m(\theta_c, \phi_c)]^* \right. \\ &\quad \left. + u_a A_n(\alpha_a) [Y_n^m(\theta_a, \phi_a)]^* \right\}. \end{aligned} \quad (38)$$

### C. Network representation

Equation (35) allows an approximation of the aperture volume velocity for wavelengths large compared to the aperture size by relating the self-and mutual impedances of the vibrating cap and aperture to each other. Additional simplification follows by representing each impedance as a lumped-element component. The lumped-element representation is particularly beneficial for estimating the Helmholtz resonance of the cavity and understanding the low-frequency behavior of the aperture volume velocity.

For long wavelengths, the small-argument approximation of the ratio<sup>29</sup>

$$\frac{h_n^{(2)}(ka)}{h_n^{(2)'}(ka)} \approx \frac{-ka}{n+1}, \quad ka \ll 1 \quad (39)$$

in Eq. (30) yields

$$\begin{aligned} Z_{A,11}^+ &\approx \tilde{Z}_{A,11}^+ \\ &= \frac{i4\pi a^3 z_0 k}{S_1^2} \sum_{n=0}^{\infty} \frac{A_n^2(\alpha_1)}{(2n+1)(n+1)} \\ &= \frac{i\omega \rho_0 l_1^+}{S_1}, \end{aligned} \quad (40)$$

where  $\tilde{Z}$  indicates a lumped-element impedance approximation and

$$l_1^+ = \frac{4\pi a^3}{S_1} \sum_{n=0}^{\infty} \frac{A_n^2(\alpha_1)}{(2n+1)(n+1)} \quad (41)$$

is the exterior end correction. Thus, the exterior self-impedance of the vibrating cap involves only an acoustic mass-like element.

The acoustic impedance of the same cap looking in to the cavity involves both acoustic compliance and acoustic mass elements in series. The compliance stems from the  $n=0$  expansion term, whereas the mass follows from the  $n>0$  terms. The  $n=0$  term reduces by applying small-argument approximations to the spherical Bessel functions,<sup>29</sup> such that

$$\frac{j_0(ka)}{j_0'(ka)} \approx \frac{-3}{ka} \quad (42)$$

and Eq. (31) becomes

$$\begin{aligned} \frac{-i4\pi a^2 z_0 j_0(ka)}{S_1^2 j_0'(ka)} A_0^2(\alpha_1) &\approx \frac{i12\pi a z_0 A_0^2(\alpha_1)}{k S_1^2} \\ &= \frac{i3\rho_0 c^2}{4\pi a^3 \omega}, \end{aligned} \quad (43)$$

since  $A_0(\alpha_1) = \frac{1}{2}(1 - \cos \alpha_1)$  and  $S_1^2 = 2\pi a^2(1 - \cos \alpha_1)$ . The terms for  $n > 0$  reduce through the approximation

$$\frac{j_n(ka)}{j_n'(ka)} \approx \frac{ka}{n}, \quad ka \ll 1, n > 0, \quad (44)$$

such that

$$\begin{aligned} \frac{-i4\pi a^2 z_0}{S_1^2} \sum_{n=1}^{\infty} \frac{j_n(ka)}{j_n'(ka)} \frac{A_n^2(\alpha_1)}{(2n+1)} \\ \approx \frac{-i4\pi a^3 k z_0}{S_1^2} \sum_{n=1}^{\infty} \frac{A_n^2(\alpha_1)}{n(2n+1)} \\ = \frac{-i\omega\rho_0 l_1^-}{S_1}, \end{aligned} \quad (45)$$

where  $l_1^-$  is the interior end correction

$$l_1^- = \frac{4\pi a^3}{S_1} \sum_{n=1}^{\infty} \frac{A_n^2(\alpha_1)}{n(2n+1)}. \quad (46)$$

Combining both terms yields

$$Z_{A,11}^- \approx \tilde{Z}_{A,11}^- = -\frac{\rho_0 c^2}{i\omega V} - \frac{i\omega\rho_0 l_1^-}{S_1}, \quad (47)$$

where  $V = 4\pi a^3/3$  is the sphere's volume. Interestingly, only the acoustic mass depends on the cap cone half angle  $\alpha_1$ . The negative signs appearing in Eq. (47) result from the definition of the normal direction of the sphere. For example, at very low frequencies where the acoustic compliance dominates, a negative cap velocity should lead to a compression in the cavity.

The mutual impedances simplify in a similar manner. On the exterior side,

$$Z_{A,12}^+ \approx \tilde{Z}_{A,12}^+ = \frac{i\omega\rho_0 l_{12}^+}{S_2}, \quad (48)$$

which is again mass-like, with an exterior mutual end correction

$$l_{12}^+ = \frac{4\pi a^3}{S_1} \sum_{n=0}^{\infty} P_n(\cos \Theta_{12}) \frac{A_n(\alpha_1)A_n(\alpha_2)}{(2n+1)(n+1)}. \quad (49)$$

The mutual impedance inside the sphere incorporates an acoustic compliance and mass in series,

$$Z_{A,12}^- \approx \tilde{Z}_{A,12}^- = -\frac{\rho_0 c^2}{i\omega V} - \frac{i\omega\rho_0 l_{12}^-}{S_2}, \quad (50)$$

where the interior mutual end correction is

$$l_{12}^- = \frac{4\pi a^3}{S_1} \sum_{n=1}^{\infty} P_n(\cos \Theta_{12}) \frac{A_n(\alpha_1)A_n(\alpha_2)}{n(2n+1)}. \quad (51)$$

Figure 2 plots the normalized self-acoustic reactances on the exterior and interior and exterior sides of a vibrating cap on a sphere with cone half angle  $\alpha_1 = 10^\circ$ . The solid black curves represent the values from the expansions given in Eqs. (30) and (31). The dashed red curves represent the low-frequency approximations from Eqs. (43) and (47). For the exterior reactance, the low-frequency approximation remains reasonable even for  $ka > 1$ ; however, the presence of modes within the spherical cavity limit the low-frequency approximation for the interior reactance.

#### D. Aperture volume velocity

Using the lumped-element impedance representations in Eq. (35) produces the following estimate for the aperture volume velocity:

$$\tilde{U}_a = -U_c \left[ \frac{S_a - k^2 V (l_{ac}^+ + l_a^-)}{S_a - k^2 V (l_a^+ + l_{ac}^-)} \right], \quad (52)$$

where  $l_{ac}^\pm$  are the mutual end corrections between the cap and aperture and  $l_a^\pm$  are the end corrections for the aperture. In the case that  $ka \ll \ll 1$  the aperture volume velocity becomes

$$\tilde{U}_a = -U_c. \quad (53)$$

Thus, as one may anticipate from near-incompressible flow at low-frequencies, the fluid externally displaced by the vibrating cap equals the fluid entering through the aperture. This equation consequently verifies Weinreich's "sound hole sum rule"<sup>22</sup> for this spherical geometry and leads to a strong dipole moment at these frequencies (see Sec. III E).

Finally, from Eq. (52) one can estimate the Helmholtz resonance frequency in terms of the lumped element

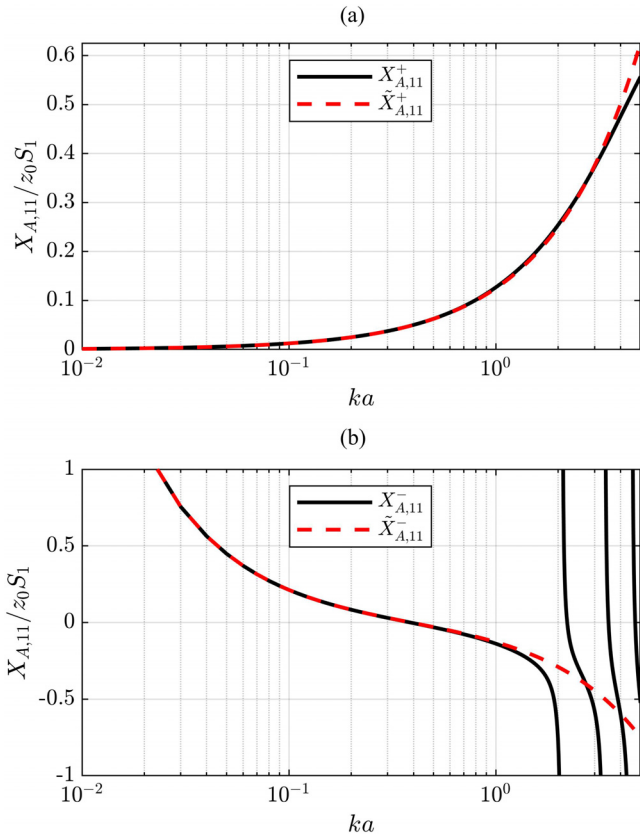


FIG. 2. (Color online) Self-acoustic reactances of a vibrating cap on a closed sphere: (a) external side and (b) internal side. The red dashed curves represent low-frequency approximations.

parameters by solving for the zero of the denominator. From Eq. (35) it is apparent that the zero occurs when  $Z_{A,a}^+ = Z_{A,a}^-$ . Applying the lumped-element values yields the Helmholtz resonance frequency<sup>35</sup>

$$\tilde{f}_H = \frac{c}{2\pi} \sqrt{\frac{S_a}{V(l_a^+ + l_a^-)}} \quad (54)$$

This equation highlights the importance of including the cavity inertance, represented by the interior end correction  $l_a^-$ , for predicting  $f_H$ .<sup>36</sup>

Figure 3 plots the magnitude and phase of the aperture volume velocity for the parameters  $\alpha_c = 10^\circ$ ,  $(\theta_c, \phi_c) = (90^\circ, 0^\circ)$ ,  $\alpha_a = 12^\circ$ ,  $(\theta_a, \phi_a) = (90^\circ, 180^\circ)$ , and  $u_c = 1$  mm/s. The blue curve presents the aperture volume velocity calculated from Eq. (35), whereas the green dashed curve shows the lumped-element prediction of the volume velocity from Eq. (52). The horizontal black dash-dot line indicates the volume velocity of the cap  $U_c$ , and the vertical red dotted line shows the estimated Helmholtz resonance frequency  $\tilde{f}_H$  from the lumped-element parameters. The insert on the magnitude plot shows results near the Helmholtz resonance.

For very small  $ka$ , both  $U_a$  and  $U_c$  converge to the same magnitude value but are  $180^\circ$  out of phase as described by Eq. (53). As frequency increases, the magnitude has a sharp peak very near  $\tilde{f}_H$ , at which point the aperture volume

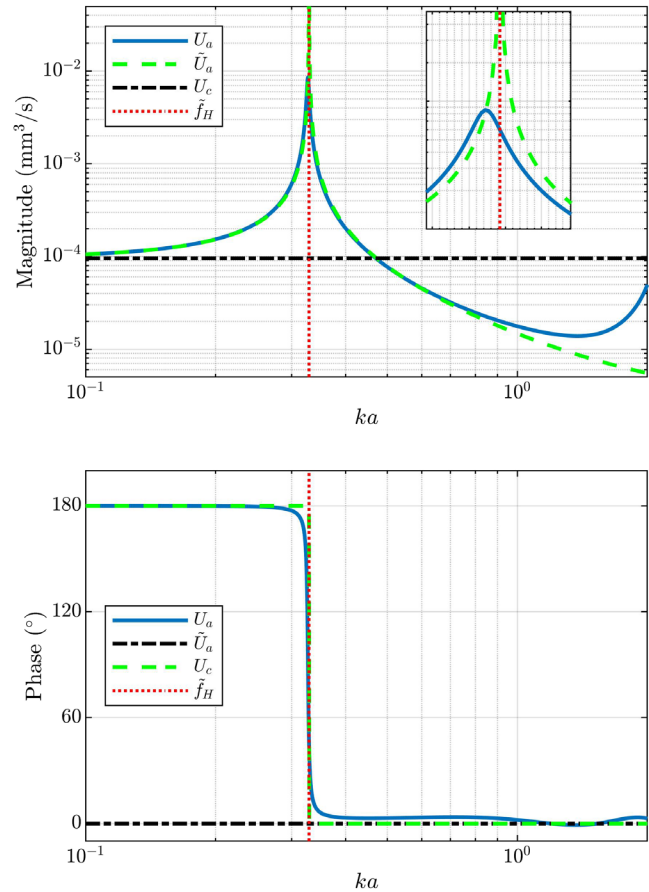


FIG. 3. (Color online) Magnitude and phase of the aperture volume velocity. The inset shows magnitude results near the Helmholtz resonance.

velocity changes to being in phase with the cap volume velocity. The wave-based self- and mutual impedances used to calculate  $U_a$  in Eq. (35) include both resistive and reactive components and thus incorporate radiation losses. However, the lumped element approximations used to calculate  $\tilde{U}_a$  do not. As a result,  $|U_a|$  does not become singular at  $\tilde{f}_H$  unlike  $|\tilde{U}_a|$ . Additionally, the incorporation of some radiation losses in  $U_a$  lowers the actual Helmholtz resonance  $f_H$  from the lumped-element estimate  $\tilde{f}_H$ .

Above  $\tilde{f}_H$ , the lumped-element representation predicts that  $|\tilde{U}_a|$  from Eq. (52) will continue to decrease; however, the curve representing  $|U_a|$  from Eq. (35) shows that after dropping below  $|U_c|$ ,  $|U_a|$  increases again. Nonetheless, the results suggest that for  $ka < 1$ , the lumped-element approximation  $\tilde{U}_a$  gives a reasonable approximation to  $U_a$ . This simplification may be beneficial for other cavity geometries where the exact forms of the self- and mutual impedances are unknown but one may estimate parameters such as cavity volume, surface area, and end-corrections.

### E. Multipole moments

At low frequencies, it is possible to predict the directional behavior of the source by considering its multipole representation.<sup>28</sup> The multipole expansion follows from a Taylor series approximation of the Green's function

employed in the Kirchhoff Helmholtz integral theorem. This allows computation of the monopole, dipole, and higher-order moments from surface integrals based on the known pressure and normal particle velocity on the boundary.<sup>28,37</sup>

For example, the monopole moment is

$$M = iz_0ka^2 \int_0^{2\pi} \int_0^\pi u_n(\theta, \phi) \sin \theta d\theta d\phi, \quad (55)$$

where  $u_n(\theta, \phi)$  is the normal component of the surface velocity [see Eq. (1)] and the dipole moment is

$$\mathbf{D} = a^2 \int_0^{2\pi} \int_0^\pi [iz_0kau_n(\theta, \phi) + p(\theta, \phi)] \hat{\mathbf{r}} \sin \theta d\theta d\phi, \quad (56)$$

where  $\hat{\mathbf{r}} = (x, y, z)/r$  is the unit vector in the direction of  $\mathbf{r}$ . Based on these two moments, the resultant field is then

$$p(\mathbf{r}) \approx p_m(\mathbf{r}) + p_d(\mathbf{r}), \quad (57)$$

where

$$p_m(\mathbf{r}) = M \frac{e^{-ikr}}{4\pi r} \quad (58)$$

and

$$p_d(\mathbf{r}) = ik \frac{e^{-ikr}}{4\pi r} \left(1 - \frac{i}{kr}\right) \mathbf{D} \cdot \hat{\mathbf{r}}. \quad (59)$$

Because of the similarity between the multipole sources and the spherical wave functions comprised of spherical harmonics and spherical Hankel functions, it is possible to assign values of the expansion coefficients to respective multipole moments.<sup>38,39</sup> However, only in the limit of  $ka \ll 1$  do the relations between the expansion coefficients and the values produced by the surface integrals in Eqs. (55) and (56) become equal.

Consider the monopole moment  $M = iz_0kU_m$ , where  $U_m$  is the equivalent monopole source strength (volume velocity). By equating terms in the spherical harmonic expansion to the pressure field of Eq. (58), it is evident that<sup>39</sup>

$$U_m = \frac{\sqrt{4\pi}}{z_0k^2} G_0^0(k). \quad (60)$$

By substituting the value for  $G_n^m(k)$  from Eq. (38) and using  $Y_0^0(\theta, \phi) = 1/\sqrt{4\pi}$  and  $S_i = 4\pi a^2 A_0(\alpha_i)$ , one arrives at the result

$$U_m = \frac{-i(U_c + U_a)}{(ka)^2 h_0^{(2)'}(ka)}. \quad (61)$$

If  $ka \ll 1$ , then the derivative of the spherical Hankel function simplifies the expression further so that

$$U_m \approx U_c + U_a. \quad (62)$$

This result shows that for long wavelengths, the equivalent monopole volume velocity is the net volume velocity on the

spherical surface as shown by Eq. (55). Because of the results in Sec. III D, when  $ka \ll \ll 1$ ,  $U_m \rightarrow 0$  and the monopole moment vanishes.

Similarly, the source's dipole moment follows by equating terms from the dipole pressure expression and the expansion components. Because the dipole moments in the  $\hat{\mathbf{x}}$  and  $\hat{\mathbf{y}}$  directions both contribute to the positive and negative-order spherical harmonic of degree one, it is convenient to express the relation to the expansion coefficients using the matrix form<sup>40</sup>

$$\begin{bmatrix} D_x \\ D_y \\ D_z \end{bmatrix} = \frac{i\sqrt{6\pi}}{k^2} \begin{bmatrix} 1 & 0 & -1 \\ -i & 0 & -i \\ 0 & \sqrt{2} & 0 \end{bmatrix} \begin{bmatrix} G_1^{-1} \\ G_1^0 \\ G_1^1 \end{bmatrix}. \quad (63)$$

While this result describes the most general relation between the degree-one expansion coefficients and the dipole moment, it is worthwhile to consider the special case where the cap and aperture align on the z-axis [i.e.,  $(\theta_c, \phi_c) = (0^\circ, 0^\circ)$  and  $(\theta_a, \phi_a) = (180^\circ, 0^\circ)$ ]. Then by symmetry, the dipole components  $D_x$  and  $D_y$  become zero and the z-component of the dipole moment becomes

$$D_z = \frac{3\pi z_0}{h_1^{(2)'}(ka)k^2} (u_c \sin^2 \alpha_c - u_a \sin^2 \alpha_a), \quad (64)$$

where the development used  $A_1(\alpha_i) = 3/4 \sin^2 \alpha_i$  and  $Y_1^0(\theta, \phi) = \sqrt{3/4\pi} \cos(\theta)$ . For  $ka \ll 1$ , the expression simplifies further to

$$D_z \approx iz_0k \frac{3\pi a^3}{2} (u_c \sin^2 \alpha_c - u_a \sin^2 \alpha_a). \quad (65)$$

This term relates directly to Eq. (56) in the following manner. Suppose the dipole moment results from a single vibrating cap of angle  $\alpha_c$ , oriented at  $(\theta_c, \phi_c) = (0, 0)$ , and with constant normal velocity  $u_i$ . The integral of Eq. (56) splits into two integrals, one for the normal component of the particle velocity and one for the pressure. The first integral becomes

$$I_1 = iz_0k2\pi a^3 u_c \int_0^{\alpha_c} \cos \theta \sin \theta d\theta \quad (66)$$

$$= iz_0k u_c \pi a^3 \sin^2 \alpha_c, \quad (67)$$

where  $z = a \cos \theta$ . For the second integral, one must use the entire expansion of Eq. (15) for the pressure. However, because the z component of the sphere's unit normal vector is  $\hat{z} = \cos \theta = \sqrt{3/4\pi} Y_0^1(\theta, \phi)$ ,<sup>40</sup> only the  $U_0^1$  term remains due to orthogonality, such that

$$I_2 = -i4\pi z_0 a^2 \frac{h_1(ka)}{3h_1^{(2)'}(ka)} u_i A_1(\alpha_i) \frac{3}{4\pi} \quad (68)$$

$$= iz_0ka^3 \frac{\pi}{2} u_i \sin^2 \theta, \quad (69)$$

provided that  $ka \ll 1$ . Thus, the total moment for a single cap becomes

$$L_i = iz_0k \frac{3\pi a^3}{2} u_i \sin^2 \alpha_i, \quad (70)$$

from which one can generalize that for  $N$  caps, each directed toward  $\hat{\mathbf{r}}_i$ ,

$$\mathbf{D} = \sum_{i=1}^N \hat{\mathbf{r}}_i L_i, \quad ka \ll 1. \quad (71)$$

Substituting appropriate values of  $\hat{\mathbf{r}}_i$  and  $L_i$  for the cap and aperture aligned on the  $z$  axis yields

$$\mathbf{D} = (L_c - L_a) \hat{\mathbf{z}}, \quad ka \ll 1, \quad (72)$$

which is equivalent to Eq. (65).

### F. Radiated sound power

Once the expansion coefficients  $G_n^m$  are known, the time-averaged sound power radiated by the source relates as<sup>39</sup>

$$\langle W(k) \rangle_t = \frac{1}{2z_0k^2} \sum_{n=0}^{\infty} \sum_{m=-n}^n |G_n^m(k)|^2. \quad (73)$$

The power radiated by the  $n=0$  term, associated with the monopole moment, is

$$\langle W(k) \rangle_t^{(m)} = \frac{z_0k^2 |U_m|^2}{8\pi}, \quad (74)$$

which tends to 0 for low frequencies since  $U_m$  vanishes. The power radiated from the  $n=1$  terms, associated with the dipole moment, is

$$\langle W(k) \rangle_t^{(d)} = \frac{k^2}{24\pi z_0} \sum_{\mu=1}^3 |D_{\mu}|^2. \quad (75)$$

When the cap and aperture are aligned on the  $z$  axis, the expression simplifies to

$$\langle W(k) \rangle_t^{(d)} \approx \frac{z_0 3\pi (ka)^4}{32} |u_c a \sin^2 \alpha_c - u_a a \sin^2 \alpha_a|^2. \quad (76)$$

Finally, when the cap and aperture have the same size ( $\alpha_c = \alpha_a$ ) and in the case that  $ka \ll \ll 1$  so  $u_c = -u_a$ ,

$$\langle W(k) \rangle_t^{(d)} \approx \frac{z_0 3\pi (ka)^4}{8} |u_c|^2 a^2 \sin^4 \alpha_c. \quad (77)$$

To illustrate these trends, Fig. 4 shows several calculated sound power level curves for an equal-sized cap and aperture ( $\alpha_c = \alpha_a = 20^\circ$ ) placed on opposing sides  $[(\theta_c, \phi_c) = (90^\circ, 0^\circ)$  and  $(\theta_a, \phi_a) = (90^\circ, 180^\circ)]$  of a sphere of radius  $a = 1$  m, with cap particle velocity  $u_c = 1.0$  mm/s. The black curve shows the total sound power level calculated from Eq. (73). The green dotted line indicates the contribution from the monopole-associated term  $n=0$

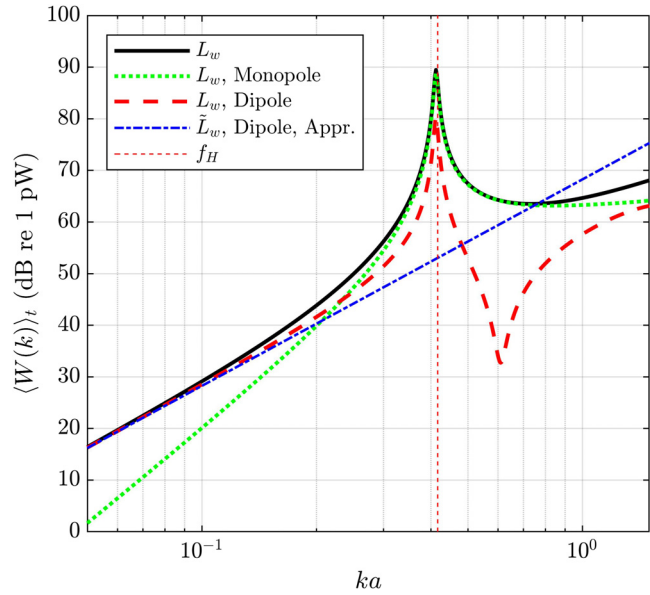


FIG. 4. (Color online) Calculated sound power levels of vibrating cap on a rigid spherical shell with a circular aperture on the opposing side.

[Eq. (74)], and the red dashed line indicates the contribution from the dipole-associated terms with  $n=1$  [Eq. (75)]. Finally, the blue line shows the low-frequency approximation for the dipole term from Eq. (77).

With the sound power contribution of the monopole and dipole moments separated, it is possible to predict the directional nature of the source qualitatively, provided that the aperture size is small enough that all assumptions remain valid. Well below the Helmholtz resonance frequency, indicated by the vertical red dotted line in Fig. 4, most of the radiated sound power is from the dipole term, such that dipolar radiation is likely. As frequency approaches the Helmholtz resonance frequency, the directivity becomes more monopolar. Finally, above resonance, the relative contributions of the monopole and dipole terms vary, suggesting more complex directivity patterns.

## IV. THEORETICAL RESULTS

### A. Comparison with BEM results

A BEM implementation of Eq. (23) allows a numerical validation of the low-frequency approximation. Figure 5 shows area-weighted directivity factor function deviation levels<sup>41</sup>  $L_Q$  between the BEM solution and the low-frequency approximation for three different  $\Theta_{ca}$  values and  $\alpha_c = \alpha_a = 18^\circ$ . For  $ka < 1$ , the low-frequency approximation and BEM solution show excellent agreement; a frequency-averaged deviation over this range is less than 0.1 dB. For  $ka > 1$ , the deviations depend upon  $\Theta_{ca}$ . When the cap and aperture are on opposing sides of the sphere ( $\Theta_{ca} = 180^\circ$ ), they are generally small, remaining below 1.0 dB up to at least  $ka = 10$ . However, when  $\Theta_{ca} = 90^\circ$  or  $\Theta_{ca} = 135^\circ$ , deviations greater than 1 dB occur above  $ka = 3$ . When the cap and aperture align, only axisymmetric particle velocity distributions occur at the aperture surface;

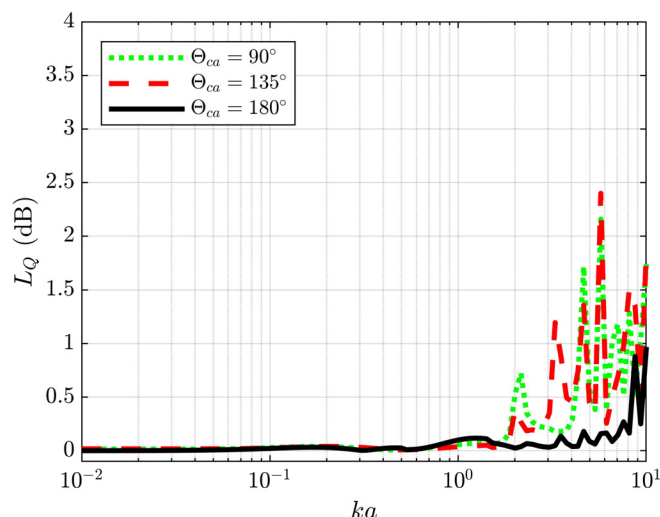


FIG. 5. (Color online) Directivity factor deviation levels  $L_Q$  between a BEM solution and the low-frequency approximation.

thus, one may anticipate that reasonable agreement follows by modeling the aperture as a cap with constant velocity. However, when the cap and aperture do not align, the aperture surface may coincide with nodal lines inside the sphere, leading to a nonaxisymmetric velocity distribution on its surface. Accordingly, the simple assumption of constant velocity over the aperture becomes less reliable, leading to larger deviations for  $ka > 1$ .

### B. General directional trends

To illustrate the general directional trends, Fig. 6 shows directivity balloons based on the low-frequency model with  $\alpha_c = \alpha_a = 18^\circ$ ,  $(\theta_c, \phi_c) = (90^\circ, 0^\circ)$ , and  $(\theta_a, \phi_a) = (90^\circ, 180^\circ)$  for selected  $ka$  values. Color and radius both indicate the levels on a decibel scale. Assuming the cap center represents the front of the sphere, the vantage point is upward and to the sphere's right. As anticipated, the directional characteristics are essentially dipolar for very small  $ka$ , as shown by Fig. 6(a); the dipole moment aligns with the cap and aperture. However, as the frequency approaches the Helmholtz resonance frequency, the strong dipolar characteristics weaken, and the directivity becomes more ellipsoidal or bean-shaped, as suggested by Fig. 6(b). At the Helmholtz resonance frequency, there is increased volume velocity at the aperture, and the directivity is essentially monopolar, as suggested by Fig. 6(c). Above resonance, the directivity patterns take on forms similar to those produced by a cap on a rigid closed sphere, such as Fig. 6(e), with reduced levels behind the sphere. However, radiation from the aperture does cause differing patterns from the closed-sphere case, such as the mushroom-like directivity patterns seen in Fig. 6(f).

Figure 7 plots the maximum directivity index (DI)<sup>10</sup> value over the sphere to quantify these directional trends over  $ka$  for the same source [ $\alpha_c = \alpha_a = 18^\circ$ ,  $(\theta_c, \phi_c) = (90^\circ, 0^\circ)$ , and  $(\theta_a, \phi_a) = (90^\circ, 180^\circ)$ ]. For an omnidirectional source, the DI is 0 dB while for a dipole source,

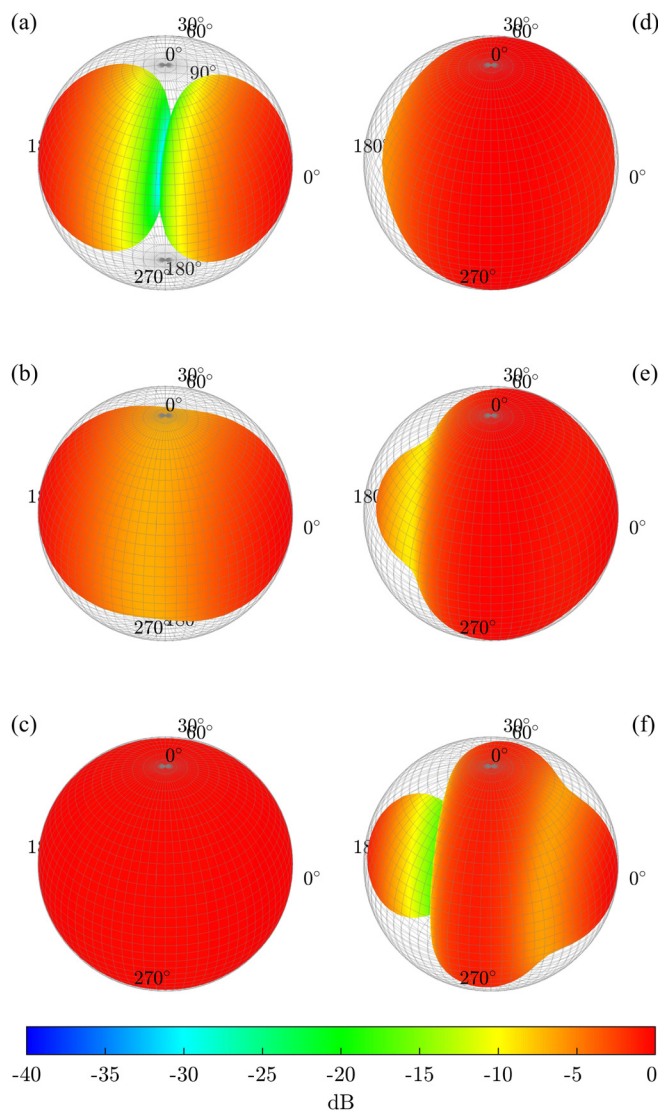


FIG. 6. (Color online) Far-field directivity balloons for a vibrating cap on a rigid spherical shell and a circular aperture on the opposing side. The results, based on the low-frequency model, are for (a)  $ka = 0.1$ , (b)  $ka = 0.2$ , (c)  $ka = 0.4$  (near the Helmholtz resonance frequency), (d)  $ka = 1$ , (e)  $ka = 1.5$ , and (f)  $ka = 2$ .

$D(\theta, \phi) \propto \cos \theta$  so that the corresponding DI value is  $10 \log_{10} 3 \approx 4.77$  dB. The overlaid horizontal dash-dot and dotted lines indicate these values, respectively. At very low frequencies, the maximum DI of the source converges to a value corresponding to dipole radiation, consistent with the results presented in Figs. 4 and 6. As the frequency approaches the Helmholtz resonance, indicated by the vertical dashed line, the DI decreases to a value corresponding to monopole radiation. Finally, above the Helmholtz resonance, the maximum DI value increases again, consistent with the more complex patterns seen in Fig. 6.

### C. Effect of aperture location

The aperture's relative size and location determine the source's dipole moment at low frequencies. Figure 8 shows far-field polar directivities in the transverse plane when

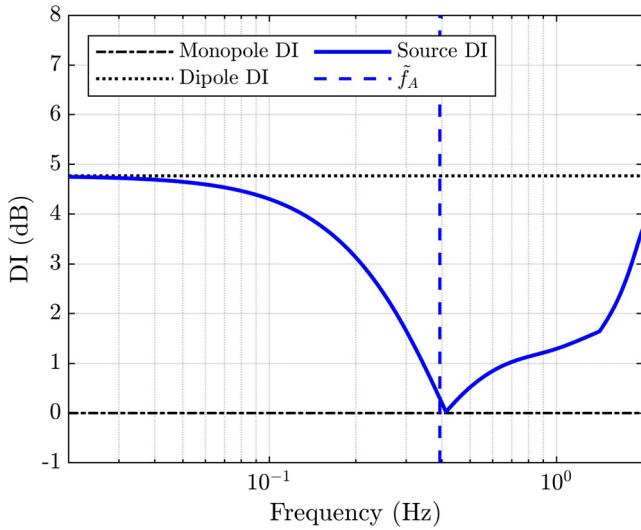


FIG. 7. (Color online) Maximum DI over the sphere for a vibrating cap on a rigid spherical shell and a circular aperture on the opposing side.

$ka = 0.001$ ,  $\alpha_c = 20^\circ$ ,  $(\theta_c, \phi_c) = (90^\circ, 0^\circ)$ , and  $\alpha_a = 5^\circ$ . The aperture location varies in six steps from  $(\theta_a, \phi_a) = (90^\circ, 180^\circ)$  (the opposing side of the sphere from the cap) to  $(\theta_a, \phi_a) = (90^\circ, 270^\circ)$  (the right side of the sphere). In each plot, the blue line indicates  $(\theta_c, \phi_c)$  and the red line indicates  $(\theta_a, \phi_a)$ . The green-dotted line denotes the pattern's null, which falls between  $(\theta_c, \phi_c)$  and  $(\theta_a, \phi_a)$ . The results show how the aperture location alters the source's directivity pattern so that the maximum radiation direction may not align with the direction of the vibrating cap.

### V. EXPERIMENTAL VALIDATION

A 3D-printed spherical loudspeaker of exterior radius  $a = 12$  cm and 5 mm wall thickness served as a tool to experimentally validate the directional characteristics of the theoretical model. The loudspeaker included a single driver positioned at  $(\theta_c, \phi_c) = (90^\circ, 0^\circ)$  with a 7 cm effective radiating diameter and cap angle  $\alpha_c \approx 36^\circ$ . In addition to the spherical loudspeaker's  $\alpha_a \approx 33^\circ$  aperture at  $(\theta_a, \phi_a) = (90^\circ, 0^\circ)$ , two variable-sized ( $\alpha_a \approx 15^\circ$  and  $\alpha_a \approx 23^\circ$ ), open spherical shell segments attach to the back and allow a total of three different aperture sizes. A 1.17 m radius rotating microphone array with 36 12.7 mm (0.5 in.) microphones measured the directivity in  $5^\circ$  resolution in both the polar and azimuthal angles, consistent with the AES sampling standard.<sup>42</sup> The array omitted the nadir (south pole) measurement position because of the obstruction caused by the loudspeaker support structure. Figure 9 shows the spherical loudspeaker (black) in the measurement system with one of the spherical shell segments (white) attached.

The experimental spherical source embodiment involved several inconsistencies with the theoretical model. First, it employed a cone loudspeaker rather than an ideal radially vibrating cap. Second, its shell had a finite rather than infinitesimal thickness. Third, to accommodate an interchanging of various fittings, the aperture has a flat

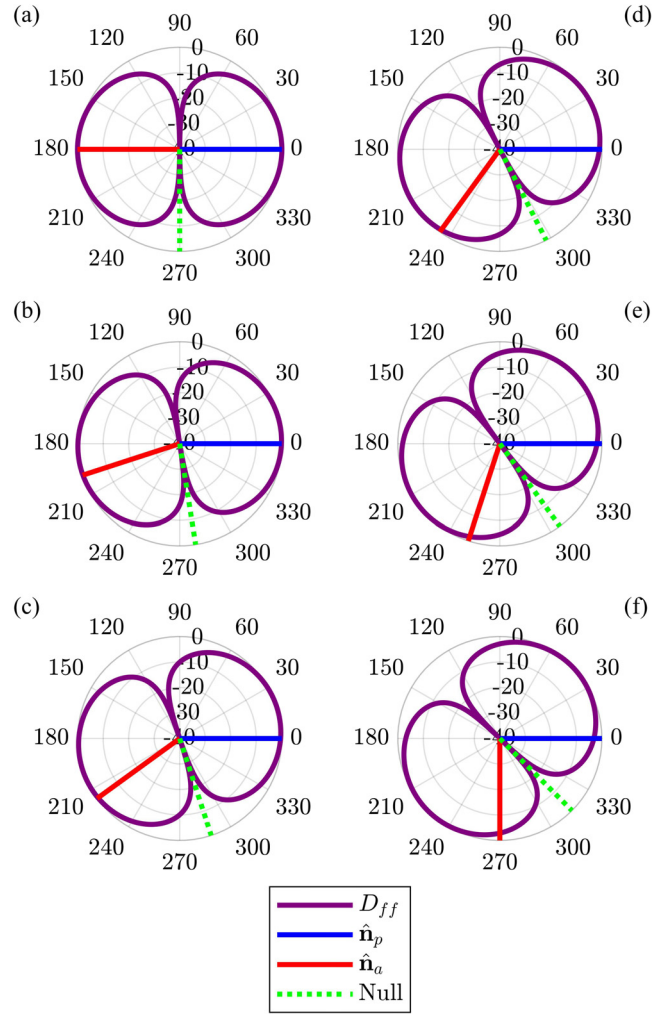


FIG. 8. (Color online) Far-field directivity of a vibrating cap on a spherical cap for  $(\theta_a, \phi_a) =$  (a)  $(90^\circ, 180^\circ)$ , (b)  $(90^\circ, 198^\circ)$ , (c)  $(90^\circ, 216^\circ)$ , (d)  $(90^\circ, 234^\circ)$ , (e)  $(90^\circ, 252^\circ)$ , (f)  $(90^\circ, 270^\circ)$ .

baffle rather than a curved baffle. These practical limitations created some ambiguity in establishing the proper values for the sphere radius  $a$  and aperture angle  $\alpha_a$ . However, rather than considering separate interior and exterior values for these parameters, the averaged value yielded a reasonable approximation.

Figure 10 shows the spherically averaged<sup>21</sup> frequency-response function between the electrical input signal and the array microphones for the three different aperture areas over a frequency range near the Helmholtz resonance frequency. The vertical dashed lines indicate the estimated  $f_H$  frequencies using Eq. (54). In all cases, the predicted resonance frequencies are less than 5% from the measured values.

Two additional vertical lines, labeled as  $f_{A1}$  and  $f_{A2}$ , indicate the first two air resonance frequencies of a closed, rigid cavity. Peaks in the spherical loudspeaker response are evident just above these values. The smaller the aperture size, the closer the measured resonance frequencies approach the rigid, closed-cavity values.

A small resonance peak appears near  $ka = 1$ . Because numerical finite-element method (FEM) simulations of the



FIG. 9. (Color online) Directivity measurement system assessing the radiation of a spherical loudspeaker positioned at its center. The white disk controls the aperture size.

plastic spherical enclosure suggest structural resonances in this spectral region, the resonance is likely due to either structural cavity properties or an electro-acoustic resonance of the driver. The preceding developments have already accounted for the Helmholtz and higher acoustic resonances, and the smaller resonance was not visible in the rigid-walled BEM simulations.

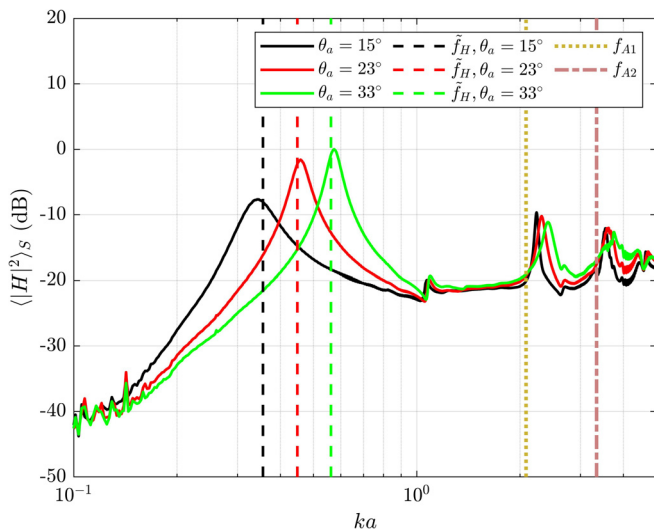


FIG. 10. (Color online) Spherically averaged magnitude response of the spherical loudspeaker with three distinct aperture sizes. The vertical lines show estimated Helmholtz and closed-cavity air resonance frequencies.

Figure 11 plots several modeled and measured source directivities at 100 Hz ( $ka = 0.2$ ) for the three aperture sizes. The directivity is nearly omnidirectional for the smallest size because the measurement frequency is close to its measured Helmholtz resonance frequency  $f_H = 159$  Hz ( $\tilde{f}_H = 165$  Hz). As the aperture sizes increase, the resonance frequencies shift higher to 213 and 267 Hz, meaning the fixed 100 Hz measurement frequency becomes relatively low, and the directivities become successively dipolar (compare Fig. 6). The levels  $L_Q$  of directivity factor function deviations between the measured and modeled patterns are 0.6, 0.4, and 0.3 dB for the smallest to largest aperture sizes, respectively. Thus, the low-frequency modeling approximations agree well with the measurements at this frequency.

Figure 12 plots modeled and measured directivities for the source at 700 Hz ( $ka = 1.5$ ). Although  $ka > 1$ , the good agreement remains between the modeled and measured directivities, with  $L_Q$  being 0.3, 0.3, and 0.4 dB for the smallest to

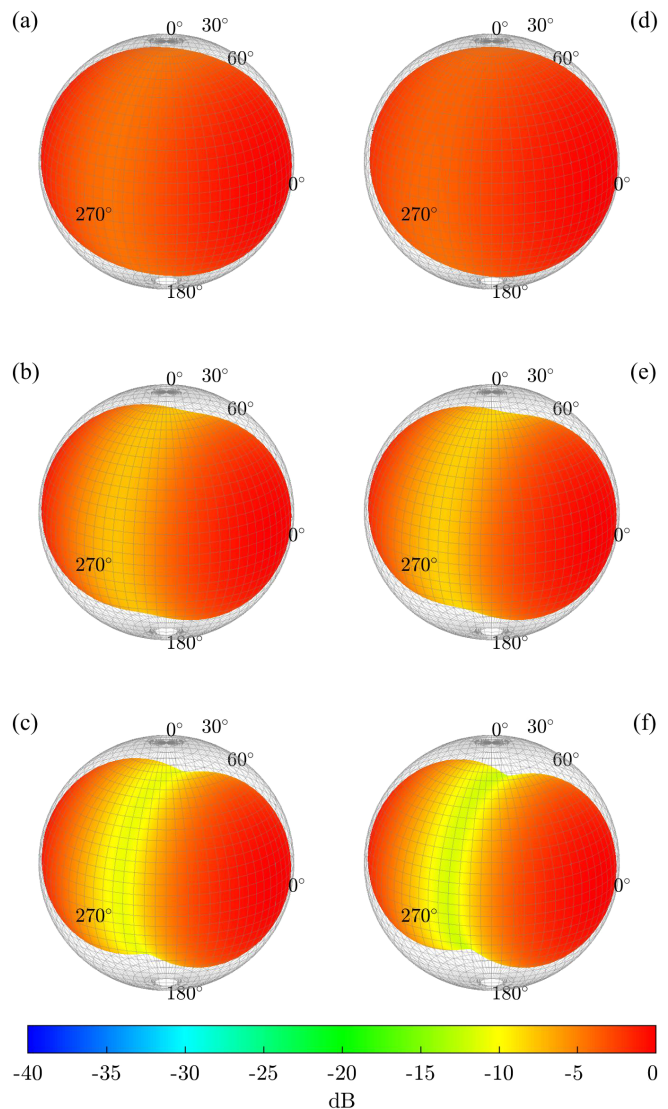


FIG. 11. (Color online) Directivity balloons at 100 Hz ( $ka = 0.2$ ) for a modeled (a)–(c) and measured (d)–(f) spherical loudspeaker with circular aperture angles (a), (d)  $\alpha_a = 15^\circ$ ; (b), (e)  $\alpha_a = 23^\circ$ ; and (c), (f)  $\alpha_a = 33^\circ$ .

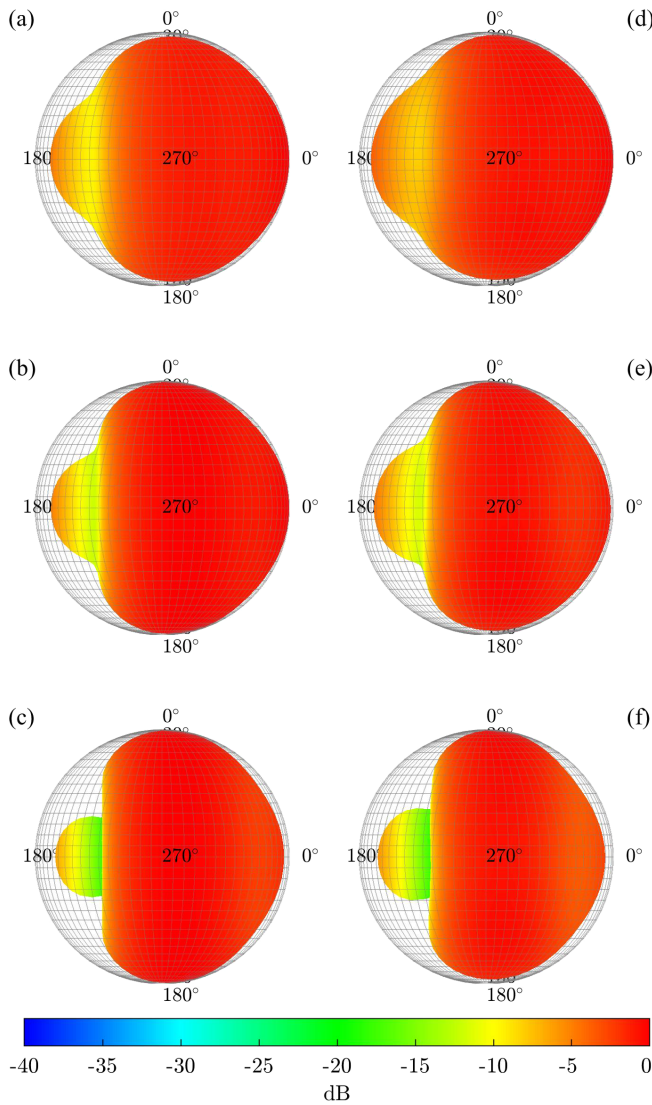


FIG. 12. (Color online) Directivity balloons at 700 Hz ( $ka = 1.5$ ) for a modeled (a)–(c) and measured (d)–(f) spherical loudspeaker with circular aperture angles (a), (d)  $\alpha_a = 15^\circ$ ; (b), (e)  $\alpha_a = 23^\circ$ ; and (c), (f)  $\alpha_a = 33^\circ$ .

largest aperture sizes, respectively. The directivity patterns are similar to the mushroom-like shapes in Fig. 6.

Figure 13 plots modeled and measured directivities for the source at 1 kHz ( $ka = 2.2$ ). More significant deviations are visible between the simulated and measured patterns at this higher frequency. The deviation level  $L_Q$  has become 1.1, 0.8, and 0.8 dB for the smallest to largest aperture sizes, respectively. However, despite the larger deviations, the essential directional characteristics remain credible for the modeled behavior. The measured directivity patterns show three distinct lobes, with substantial radiation behind the loudspeaker.

Figure 14 plots modeled and measured directivities for the source at 1.5 kHz ( $ka = 3.2$ ). As anticipated, the deviations have increased; the  $L_Q$  values are 1.5, 1.7, and 1.4 dB for the smallest to largest aperture sizes, respectively. However, a general qualitative agreement between simulated and measured directivities remains. The measured

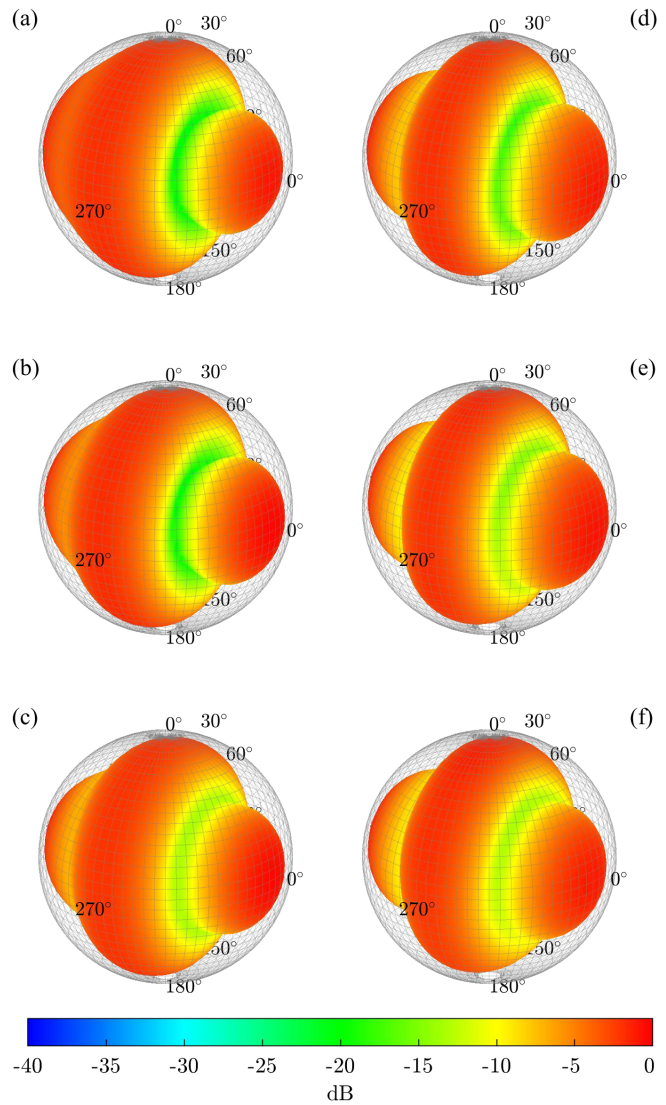


FIG. 13. (Color online) Directivity balloons at 1 kHz ( $ka = 2.2$ ) for a modeled (a)–(c) and measured (d)–(f) spherical loudspeaker with circular aperture angles (a), (d)  $\alpha_a = 15^\circ$ ; (b), (e)  $\alpha_a = 23^\circ$ ; and (c), (f)  $\alpha_a = 33^\circ$ .

directivity has a unique form with distinct lobes and a mushroom-shaped region of intense radiation directly in front of the loudspeaker driver. For the larger apertures, the most substantial radiation is behind the loudspeaker rather than in front.

## VI. ANALYSIS AND DISCUSSION

Figure 15 shows graphs of  $L_Q$  values between the simulated and measured data for each of the three aperture sizes. Figure 15(a) shows the results for simulated directivities using  $U_a$  for the aperture velocity, as derived from the self- and mutual impedances in Eq. (35). With two exceptions, the directivity deviations remain below 1.0 dB up to  $ka = 2$ . The sharp deviation peak near  $ka = 1$  corresponds to the resonance peak in Fig. 10. The smaller peak near  $ka = 0.8$  also coincides with a small bump in the black curve and, to a lesser extent, in the red curve of Fig. 10. Visual inspection of the measured directivities at these frequencies reveals a

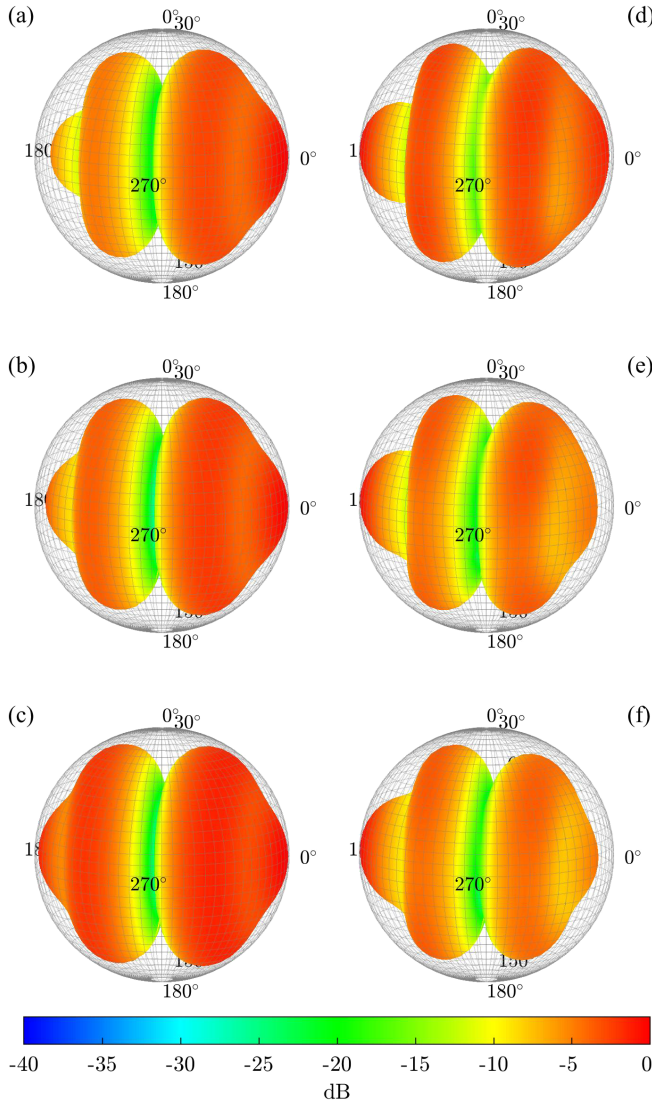


FIG. 14. (Color online) Directivity balloons at 1.5 kHz ( $ka = 3.2$ ) for a modeled (a)–(c) and measured (d)–(f) spherical loudspeaker with circular aperture angles (a), (d)  $\alpha_a = 15^\circ$ ; (b), (e)  $\alpha_a = 23^\circ$ ; and (c), (f)  $\alpha_a = 33^\circ$ .

“lumpy” characteristic to the balloons, indicative of wave interference. As discussed in Sec. V, these anomalies are likely due to structural or other resonances not accounted for in the rigid-wall model assumption. This assertion receives additional validation because the deviations occur at the same frequencies regardless of the aperture size and thus appear independent of the strictly acoustic source properties. Above  $ka = 2$ , the deviations between measurements and the model continue to grow, exceeding 3.0 dB by around  $ka = 6$ . Vertical dashed lines in the figure represent the resonance frequencies of a closed, rigid-walled sphere. Near these resonances, spikes in the deviation curves are apparent.

Figure 15(b) shows similar  $L_Q$  graphs for directivities simulated using  $\tilde{U}_a$  for the aperture velocity, as derived from lumped-element parameters in Eq. (52). The deviations for  $ka < 1$  are virtually identical to those derived from  $U_a$ . However, for  $ka > 1$ , the deviations rise to near 2.0 dB by

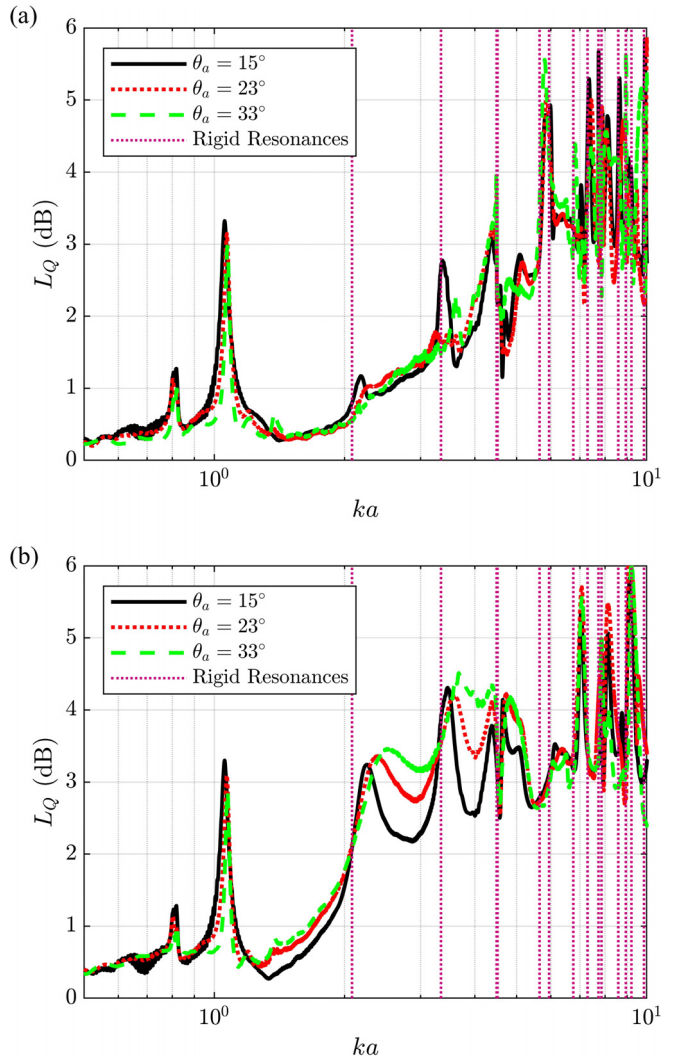


FIG. 15. (Color online) Directivity factor function deviation levels between the measured and modeled directivities with (a) aperture velocity  $U_a$  and (b) lumped-element aperture velocity approximation  $\tilde{U}_a$ .

$ka = 2.0$  and quickly rise to over 3.0 dB before  $ka = 3.0$ . As suggested by Fig. 3,  $\tilde{U}_a$  tends gradually to zero above resonance, whereas  $U_a$  rises again. Thus, using  $U_a$  over  $\tilde{U}_a$  becomes important above the source’s Helmholtz resonance frequency. Below this range,  $\tilde{U}_a$  gives a reliable estimate, which is beneficial when exact formulas for self- and mutual impedances are unknown due to differing cavity and cap shapes.

These results, the BEM deviations, and the results from Sec. V suggest the following rules of thumb. Below  $ka = 1$ , the low-frequency model quantitatively agrees well with the complete solution and measurements. In this spectral region, the lumped-element parameters reasonably estimate the aperture volume velocity so that  $\tilde{U}_a \approx U_a$ . Above  $ka = 1$ , the low-frequency approximation using  $U_a$  gives good agreement up to at least  $ka = 5$  when the cap and aperture align. However, the agreement is less reliable when the cap and aperture do not align. Additionally, above  $ka = 1$ , the

lumped-element estimate  $\tilde{U}_a$  is unreliable even when the cap and aperture align.

While the model discussed in the present work is sufficient to predict directional characteristics, the radiated sound power results appearing in Fig. 4 only apply when the rigid cap vibrates with infinite internal impedance to produce a constant, frequency-independent cap velocity. This assumption is unrealistic when applied to some acoustic sources, such as loudspeakers. Accurately predicting the total radiated energy would require properly modeling the driver's finite impedance. Finite-impedance effects are particularly significant near the Helmholtz resonance of the cavity, where the impedance on the interior side vanishes (see Fig. 2). Additionally, incorporating thermoviscous losses is necessary to predict the resonator's behavior more accurately.<sup>36</sup>

## VII. CONCLUSIONS

This work has developed a low-frequency approximation to a vibrating cap on a spherical shell with a circular aperture. The key idea has been to model the aperture as a second vibrating cap with a velocity determined by the self- and mutual impedance between the aperture and the primary vibrating cap. Lumped-element approximations of the self- and mutual impedances provided a simplified formula for the aperture volume velocity and Helmholtz resonance frequency. Multipole moments extracted from the derived spherical harmonic coefficients reveal that at very low frequencies, the directivity is dipolar. Approaching the Helmholtz resonance frequency, the directivity becomes more monopolar until it reaches a quasi-omnidirectional state at resonance. Above resonance, the directivity takes on more complex forms. Both numerical BEM simulations and measurements of a comparable spherical loudspeaker validated the low-frequency approximation, yielding good quantitative agreement in the low-frequency regime.

The model's results will be beneficial for understanding and predicting the directivities of sources with apertures, such as musical instruments with sound holes, guitar amplifiers with open backs, or loudspeakers with vents. However, specific applications of this model to these and other sources will require careful adaptations. For example, applying the model to loudspeakers would require properly representing the finite-impedance effects of the loudspeaker driver and appropriate losses. For application to musical instruments such as the guitar, the influence of the structural vibrations of the resonator body must be considered in addition to radiation through the sound hole. Because this work focused on low-frequency approximations, future research could also develop a numerical method such as MAR to obtain results valid for  $ka \gg 1$ . Other research could consider models for multiple caps and apertures.

## ACKNOWLEDGMENTS

The authors express appreciation for funding from the William James and Charlene Fuhrman Strong Family

Musical Acoustics Endowed Fellowship Fund and to Jeremy Peterson for help in constructing the spherical loudspeaker.

## AUTHOR DECLARATIONS

### Conflict of Interest

The authors declare no conflicts of interest.

## DATA AVAILABILITY

The data that support the findings of this study are available from the corresponding author upon reasonable request.

- <sup>1</sup>M. Greenspan, "Piston radiator: Some extensions of the theory," *J. Acoust. Soc. Am.* **65**, 608–621 (1979).
- <sup>2</sup>T. Mellow, "On the sound field of a resilient disk in an infinite baffle," *J. Acoust. Soc. Am.* **120**(1), 90–101 (2006).
- <sup>3</sup>R. M. Aarts and A. J. E. M. Janssen, "On-axis and far-field sound radiation from resilient flat and dome-shaped radiators," *J. Acoust. Soc. Am.* **125**(3), 1444–1455 (2009).
- <sup>4</sup>P. M. Morse, "Vibration and Sound," in *International Series in Pure & Applied Physics*, 2nd ed. (McGraw-Hill, New York, 1948).
- <sup>5</sup>P. M. Morse and K. U. Ingard, *Theoretical Acoustics* (Princeton University Press, Princeton, NJ, 1968).
- <sup>6</sup>A. Lindberg and G. Pavić, "Computation of sound radiation by a driver in a cabinet using a substitute source approach," *J. Acoust. Soc. Am.* **138**(2), 1132–1142 (2015).
- <sup>7</sup>S. D. Bellows and T. W. Leishman, "Modeling musician diffraction and absorption for artificially excited clarinet directivity measurements," *Proc. Mtgs. Acoust.* **46**(1), 035002 (2022).
- <sup>8</sup>E. Skudrzyk, *The Foundations of Acoustics* (Springer-Verlag, New York, 1971).
- <sup>9</sup>W. Williams, N. G. Parke, D. A. Moran, and C. H. Sherman, "Acoustic radiation from a finite cylinder," *J. Acoust. Soc. Am.* **36**(12), 2316–2322 (1964).
- <sup>10</sup>L. Beranek and T. Mellow, *Acoustics: Sound Fields, Transducers and Vibration*, 2nd ed. (Academic Press, New York, 2019).
- <sup>11</sup>R. M. Aarts and A. J. E. M. Janssen, "Sound radiation from a resilient spherical cap on a rigid sphere," *J. Acoust. Soc. Am.* **127**(4), 2262–2273 (2010).
- <sup>12</sup>J. L. Butler, "Solution of acoustical-radiation problems by boundary collocation," *J. Acoust. Soc. Am.* **48**(1B), 325–336 (1970).
- <sup>13</sup>C. C. Gerding and W. Thompson, "Axisymmetric spherical radiator with mixed boundary conditions," *J. Acoust. Soc. Am.* **61**(2), 313–317 (1977).
- <sup>14</sup>T. F. Johansen, "On the directivity of horn loudspeakers," *J. Audio Eng. Soc.* **42**(12), 1008–1019 (1994).
- <sup>15</sup>A. M. Pasqual and V. Martin, "On the acoustic radiation modes of compact regular polyhedral arrays of independent loudspeakers," *J. Acoust. Soc. Am.* **130**(3), 1325–1336 (2011).
- <sup>16</sup>J. Mortensen, "Computing the directivities of platonic-solid loudspeakers," Senior thesis, Brigham Young University, Provo, UT (2014).
- <sup>17</sup>M. T. Neal and M. C. Vigeant, "A compact spherical loudspeaker array for efficiently recreating instrument directivities," *J. Audio Eng. Soc.* **68**(11), 796–809 (2020).
- <sup>18</sup>T. W. Leishman, S. Rollins, and H. M. Smith, "An experimental evaluation of regular polyhedron loudspeakers as omnidirectional sources of sound," *J. Acoust. Soc. Am.* **120**(3), 1411–1422 (2006).
- <sup>19</sup>J. L. Flanagan, "Analog measurements of sound radiation from the mouth," *J. Acoust. Soc. Am.* **32**(12), 1613–1620 (1960).
- <sup>20</sup>T. Halkosaari, M. Vaalgamaa, and M. Karjalainen, "Directivity of artificial and human speech," *J. Audio Eng. Soc.* **53**(7/8), 620–631 (2005).
- <sup>21</sup>T. W. Leishman, S. D. Bellows, C. M. Pincock, and J. K. Whiting, "High-resolution spherical directivity of live speech from a multiple-capture transfer function method," *J. Acoust. Soc. Am.* **149**(3), 1507–1523 (2021).
- <sup>22</sup>G. Weinreich, "Sound hole sum rule and the dipole moment of the violin," *J. Acoust. Soc. Am.* **77**(2), 710–718 (1985).
- <sup>23</sup>J. W. Miles, "Scattering by a spherical cap," *J. Acoust. Soc. Am.* **50**(3B), 892–903 (1971).

- <sup>24</sup>G. Elias and P. Malbéqui, “Scattering by an open sphere: Exact solution and comparison with a boundary integral method,” *J. Acoust. Soc. Am.* **93**(2), 609–616 (1993).
- <sup>25</sup>A. Nosich, “The method of analytical regularization in wave-scattering and eigenvalue problems: Foundations and review of solutions,” *IEEE Antennas Propag. Mag.* **41**(3), 34–49 (1999).
- <sup>26</sup>E. D. Vinogradova, “Axisymmetric acoustic oscillations of a rigid spherical shell with two symmetric circular apertures,” *J. Sound Vib.* **503**, 116115 (2021).
- <sup>27</sup>E. A. G. Shaw, “Cavity resonance in the violin: Network representation and the effect of damped and undamped rib holes,” *J. Acoust. Soc. Am.* **87**(1), 398–410 (1990).
- <sup>28</sup>A. D. Pierce, *Acoustics* (Springer International Publishing, Cham, Switzerland, 2019).
- <sup>29</sup>T. M. Dunster, *NIST Handbook of Mathematical Functions* (Cambridge University Press, New York, 2010).
- <sup>30</sup>T. W. Wu, *Boundary Element Acoustics: Fundamentals and Computer Codes* (WIT Press, Southampton, England, 2000).
- <sup>31</sup>A. J. Burton and G. F. Miller, “The application of integral equation methods to the numerical solution of some exterior boundary-value problems,” *Proc. R. Soc. London, Ser. A: Math. Phys. Sci.* **323**(1553), 201–210 (1971).
- <sup>32</sup>P. Filippi, “Layer potentials and acoustic diffraction,” *J. Sound Vib.* **54**(4), 473–500 (1977).
- <sup>33</sup>T. W. Wu and G. C. Wan, “Numerical modeling of acoustic radiation and scattering from thin bodies using a Cauchy principal integral equation,” *J. Acoust. Soc. Am.* **92**(5), 2900–2906 (1992).
- <sup>34</sup>C. H. Sherman, “Mutual radiation impedance of sources on a sphere,” *J. Acoust. Soc. Am.* **31**(7), 947–952 (1959).
- <sup>35</sup>J. W. Strutt, *The Theory of Sound* (Cambridge University Press, Cambridge, 2011).
- <sup>36</sup>U. Ingard, “On the theory and design of acoustic resonators,” *J. Acoust. Soc. Am.* **25**(6), 1037–1061 (1953).
- <sup>37</sup>A. Chaigne and J. Kergomard, *Acoustics of Musical Instruments* (Springer, New York, 2016).
- <sup>38</sup>T. Martin and A. Roure, “Optimization of an active noise control system using spherical harmonics expansion of the primary field,” *J. Sound Vib.* **201**(5), 577–593 (1997).
- <sup>39</sup>E. G. Williams, *Fourier Acoustics: Sound Radiation and Nearfield Acoustical Holography* (Academic Press, London, 1999).
- <sup>40</sup>S. D. Bellows and T. W. Leishman, “On the low-frequency acoustic center,” *J. Acoust. Soc. Am.* **153**(6), 3404–3418 (2023).
- <sup>41</sup>S. Bellows and T. W. Leishman, “Effect of head orientation on speech directivity,” in *Proceedings of Interspeech 2022* (2022), pp. 246–250.
- <sup>42</sup>*AES56-2008 (r2019): AES Standard on Acoustics—Sound Source Modeling—Loudspeaker Polar Radiation Measurements* (Audio Engineering Society, New York, 2019).